Observations of flooding and snow-ice formation in a thinner Arctic sea ice regime during the N-ICE2015 campaign: Influence of basal ice melt and storms

Christine Provost, Nathalie Sennéchael, Jonas Miguet, Polona Itkin, Anja Rösel, Zoé Koenig, Nicolas Villacieros Robineau, Nicolas Villacieros Robineau, Mats A. Granskog

AGU PUBLICATIONS

JGR

Journal of Geophysical Research: Oceans

RESEARCH ARTICLE

10.1002/2016JC012011

Special Section:
Atmosphere-ice-ocean-ecosystem Processes in a Thinner Arctic Sea Ice Regime: The Norwegian Young Sea ICE Cruise 2015 (N-ICE2015)

Observations of flooding and snow-ice formation in a thinner Arctic sea-ice regime during the N-ICE2015 campaign: Influence of basal ice melt and storms

Christine Provost[1], Nathalie Sennéchael[1], Jonas Miguet[1], Polona Itkin[2], Anja Rösel[2], Zoé Koenig[1], Nicolas Villacieros-Robineau[1], and Mats A. Granskog[2]

[1]Laboratoire LOCEAN-IPSL, Sorbonne Universités (UPMC, Univ. Paris 6)-CNRS-IRD-MNHN, Paris, France, [2]Norwegian Polar Institute, Fram Centre, Tromsø, Norway

Abstract Seven ice mass balance instruments deployed near 83°N on different first-year and second-year ice floes, representing variable snow and ice conditions, documented the evolution of snow and ice conditions in the Arctic Ocean north of Svalbard in January–March 2015. Frequent profiles of temperature and thermal diffusivity proxy were recorded to distinguish changes in snow depth and ice thickness with 2 cm vertical resolution. Four instruments documented flooding and snow-ice formation. Flooding was clearly detectable in the simultaneous changes in thermal diffusivity proxy, increased temperature, and heat propagation through the underlying ice. Slush then progressively transformed into snow-ice. Flooding resulted from two different processes: (i) after storm-induced breakup of snow-loaded floes and (ii) after loss of buoyancy due to basal ice melt. In the case of breakup, when the ice was cold and not permeable, rapid flooding, probably due to lateral intrusion of seawater, led to slush and snow-ice layers at the ocean freezing temperature (−1.88°C). After the storm, the instruments documented basal sea-ice melt over warm Atlantic waters and ocean-to-ice heat flux peaked at up to 400 W m^{-2}. The warm ice was then permeable and flooding was more gradual probably involving vertical intrusion of brines and led to colder slush and snow-ice (−3°C). The N-ICE2015 campaign provided the first documentation of significant flooding and snow-ice formation in the Arctic ice pack as the slush partially refroze. Snow-ice formation may become a more frequently observed process in a thinner ice Arctic.

Key Points:
- We report the first direct observations of in situ snow-ice formation in the high Arctic
- Snow-ice formation occurred after storms and/or basal ice melt
- The midwinter observations document intense sea-ice basal melt over warm Atlantic waters

Correspondence to:
C. Provost,
cp@locean-ipsl.upmc.fr

Citation:
Provost, C., N. Sennéchael, J. Miguet, P. Itkin, A. Rösel, Z. Koenig, N. Villacieros-Robineau, and M. A. Granskog (2017), Observations of flooding and snow-ice formation in a thinner Arctic sea-ice regime during the N-ICE2015 campaign: Influence of basal ice melt and storms, *J. Geophys. Res. Oceans*, *122*, 7115–7134, doi:10.1002/2016JC012011.

Received 3 JUN 2016
Accepted 8 FEB 2017
Accepted article online 14 FEB 2017
Published online 6 SEP 2017

1. Introduction

Changes to the Arctic climate system are symptomatic of ongoing global climate change. These changes are magnified compared to lower latitudes and result in a smaller, thinner, and faster moving ice cover than just a decade ago [*Lindsay and Schweiger*, 2015; *Spreen et al*., 2011]. Progressive degradation of multiyear ice in the 1990s and 2000s has led to the prevalence of seasonal ice after 2007 [*Maslanik et al*., 2007]. The changes in sea-ice extent and physical structure are causing dramatic shifts in the interactions between sea-ice and both the atmosphere and the underlying ocean [e.g., *Perovich and Richter-Menge*, 2009; *Boisvert and Stroeve*, 2015]. Despite advances in numerical modeling, the reliability of present-day climate and numerical prediction models is limited in the Arctic with considerable uncertainties in the projected rates of sea-ice decline [*Overland and Wang*, 2013]. Small-scale physical processes that play an important role in the Arctic atmosphere-snow-sea-ice-ocean system, in particular at the interfaces, are not well represented in models [*Vihma et al*., 2014].

The shift of the Arctic ice pack to a predominantly thinner and seasonal one, may introduce conditions that more closely resemble the Antarctic ice pack, where the formation of snow-ice is a common process [e.g., *Eicken et al*., 1994], fostered by a relatively thin ice cover [*Worby et al*., 2008] and abundant snow fall [*Bromwich et al*., 2004]. Indeed, snow-ice formation results from the freezing of a mixture of snow and seawater produced by the flooding of ice floes. Flooding can result from negative freeboard conditions due to a heavy snow load relative to ice thickness (crack in the ice, edge of floes, permeable ice) or from capillary wicking of brines even in positive freeboard conditions [*Massom et al*., 2001; *Lewis et al*., 2011]. The slush resulting from flooding solidifies into snow-ice if a sufficient heat sink is available (cold atmosphere or/and cold underlying sea-ice). Snow-ice contributes to about a quarter of the total sea-ice

formation in the Antarctic zone as suggested by isotope analyses [*Jeffries et al*., 1997, 2001] and satellite estimates [*Maksym and Markus*, 2008]. In the high Arctic, the ratio of snow thickness to ice thickness has usually been small and snow-ice formation has not received much attention [*Vihma et al*., 2014]. Only a few observations show snow-ice formation in the central Arctic. *Tucker et al*. [1991] present observations that point toward formation of snow-ice in the winter marginal ice zone in Fram Strait. Work on landfast ice has reported variable contributions of snow-ice. *Kawamura et al*. [2001], in one of the few studies in the high Arctic, found no evidence of snow-ice in landfast ice cores taken from the North Water Polynya region in Northern Baffin Bay, while in coastal areas and marginal seas with thinner ice cover, snow contribution can be significant [e.g., *Weeks and Lee*, 1958; *Ukita et al*., 2000; *Granskog et al*., 2003; *Kirillov et al*., 2015]. Climate models project an increase in annual precipitation over the Arctic [*Overland et al*., 2012; *Bintanja and Selten*, 2014]. Larger snow fall rates after sea-ice freezeup would promote snow-ice formation. However, whether the increased precipitation will fall as snow or rain on sea-ice is still uncertain [e.g., *Hezel et al*., 2012: *Bintanja and Selten*, 2014]. Observations suggest regional differences in snow loading over the Arctic sea-ice: snow depth on first-year sea-ice has decreased in the western Arctic [*Webster et al*., 2014], while north of Svalbard there is very little snow depth data to conclude whether this is a pan-Arctic phenomena, although recent observations point to thick snow covers in this region [*Haapala et al*., 2013; *Rösel et al*., 2016]. An increase in snow precipitation together with the thinning of the sea-ice cover could result in more extensive occurrence of snow-ice, with larger contributions to total ice mass [*Granskog et al*., 2017].

The Norwegian young sea ICE (N-ICE2015) expedition [*Granskog et al*., 2016] with the research vessel Lance frozen in the Arctic ice pack provided a research platform for studying the atmosphere, snow, sea-ice, ocean and marine ecosystem throughout the Arctic winter and spring. During winter 2015, the Arctic vortex was strong with large amount of northward meridional transport over the Greenland Sea. Six synoptic events occurred bringing warm and moist air from the south, strong winds and precipitation [*Graham et al*., 2017; *Cohen et al*., 2017]. Precipitation rates based on ERA-Interim reanalysis [*Dee et al*., 2011] show that winter 2015 was exceptional in terms of snowfall. The snowfall in February 2015 was the largest in the ERA-Interim reanalysis record (1979–2015) for the N-ICE2015 region.

Here we present observations from seven ice mass balance instruments that drifted with pack ice from 83.5°N to 81°N around 16°E–18°E from mid-January to mid-March 2015. The instruments, which remained close to each other, were deployed in a wide variety of initial snow and ice thicknesses. Basal sea-ice melt in the middle of winter is observed by all the instruments and, for the first time in the high Arctic, snow-ice formation is observed in situ. The paper is organized as follows: observations and methods to derive interfaces and fluxes from the data are presented in section 2. In section 3, the evolution of the floes along the drift as documented by the seven instruments is described. Finally, section 4 summarizes the results and provides a future outlook.

2. Material and Methods

2.1. Ice Mass Balance Instruments and Deployments

The ice mass balance instruments deployed during N-ICE2015 (Table 1) were developed by the Scottish Association for Marine Science (SAMS) [*Jackson et al*., 2013]. Hereafter, we call them SIMBAs standing for SAMS ice mass balance for the Arctic. SIMBAs are equipped with a 5 m long chain cable hanging through air, snow, sea-ice and ocean comprising solid-state sensors that measure temperature profiles with 2 cm vertical resolution at approximately 0.1°C accuracy. They also feature a heating mode that provides a proxy for thermal diffusivity, which can be used to discriminate between different media, especially between snow and ice [*Jackson et al*., 2013]. Temperature was measured every 3 or 6 h, while heating with a duration of 120 s was performed once or twice per day (Table 1). During the heating mode that immediately follows one of the temperature profiles (T_0), temperature is measured after 30 and 120 s (T_1 and T_2) and the ratio of the observed temperature changes $(T_2 - T_0)/(T_1 - T_0)$ is the proxy for thermal diffusivity.

Seven SIMBAs were deployed between 15 January and 29 January (Table 1), during the first phase of the N-ICE2015 campaign using the research vessel Lance as a base for an ice station [*Granskog et al*., 2016]. The SIMBAs were typically deployed on level parts of floes, remote from immediate active sea-ice deformation processes (leads and ridges), thus they likely recorded conditions that are representative of level ice. The

Table 1. Temporal Coverage, Initial Conditions (Measured at Time of Deployment), and Sampling Frequency of the Seven SIMBAs Deployed in January During N-ICE2015[a]

	SIMBA_2015h	SIMBA_2015a	SIMBA_2015i	SIMBA_2015f	SIMBA_2015b	SIMBA_2015g	SIMBA_2015e
Drift Time							
Start	24 Jan	15 Jan	27 Jan	25 Jan	16 Jan	29 Jan	27 Jan
End	16 Mar	16 Mar	21 Feb	19 Feb	16 Feb	28 Feb	26 Feb
Record length (days)	53	61	26	27	33	30	32
Ice type	SYI	N/A	SYI	FYI	FYI[b]	FYI[b]	FYI[b]
Initial Thickness (cm)							
Snow (point)	55	47	53	43	30	36	0
Snow (area)	49 (10)	59 (9)	49 (10)	33 (14)	44 (8)	41 (3)	21 (6)
Transect length	1.7 km	30 m	1.7 km	1.2 km	30 m	15 m	15 m
Ice	155	133	119	90	134	108	152
Freeboard	2	1	−4	−1	2	2	9
Frequency (h)							
GPS	2	1	2	1	1	1	6
Temperature	3	6	3	6	6	6	6
Heating cycle	24	24	12	24	24	24	24

[a]The initial thickness of snow (point) is the value observed at the SIMBAs at deployment. The initial thickness of snow (area) is the average value and standard deviation in parentheses from nearby snow depth transect lines at deployment date. Length of transect lines varied and are indicated. Initial ice and freeboard were measured at the SIMBAs.

[b]Ice type suggested from the relatively low averaged snow depth in the vicinity of the deployment site (although snow thickness is not a reliable metrics for distinguishing sea-ice age).

typical floe size was 100–500 m in diameter. The SIMBA chain cable was mounted on a tripod or on a horizontal pole extended from an uplifted platform and a 5 cm hole was drilled through the ice through which the chain was deployed. After the deployment we attempted to reconstruct the original sea-ice thickness by adding cold fresh water into the ice hole and by carefully filling in the snow to the original level. This last step was not done in the case of SIMBA_2015e (Table 1), where we intentionally left the ice bare to observe how fast the snow cover restored itself (snow depth on that floe was 21 cm at deployment). Data (including GPS coordinates, see Figure 1a) from SIMBAs were sent by satellite at regular intervals (Table 1). The shortest distance between any pair of instruments was only about 500 m (initially on the same floe) and the largest distance never exceeded 50 km at any time (Figure 1b). All SIMBAs experienced similar drifts with hourly drift velocities that exceeded 0.2 m s^{-1} during the six major storms (M1–M6) [*Cohen et al.*, 2017] (Figure 1c). Table 1 summarizes the temporal extension, initial snow and ice conditions, and measurement setup of the SIMBAs. Most SIMBAs either stopped working or were recovered when the floe around Lance broke up on 21 February during storm M3. Two of them, however, kept functioning until 16 March. One of the latter, SIMBA_2015h, was deployed close enough to Lance to allow for periodical checks of the surface components until 21 February.

2.2. Identification of the Material Interfaces

We define the interfaces between the air/snow, snow/ice, and ice/ocean based on the temperature profiles and the thermal diffusivity proxy. SIMBA_2015h features highest temporal resolution (Table 1) and is used as an example in the subsections below. The calculated interfaces are marked in Figure 2 and they agree well with a visual interpretation of the profiles.

2.2.1. Air/Snow Interface

Diffusivity proxy alone can unfortunately not be used to reliably estimate the snow surface level due to icing (hoar frost) on the chain (Figure 2d). Instead we examined the vertical gradient of temperature and simultaneously the standard deviation over 24, 48, and 72 h period. Starting from the top of the chain we looked for a sharp increase in the vertical temperature gradient and a decrease in the standard deviation. This simple semiautomatic procedure provides a satisfying interface consistent with the time derivative of temperature and the diffusivity proxy with a rather constant snow thickness of 52 cm increasing to 88 cm on 16 February during storm M3 (Figure 2). The error range is small, about 2 cm on average, and does not exceed 6 cm at any time.

2.2.2. Snow/Ice Interface

The snow/ice interface is simple to derive from the sharp contrast in the diffusivity proxy values between both media. The snow/ice interface does not change except for slush formation associated with flooding on

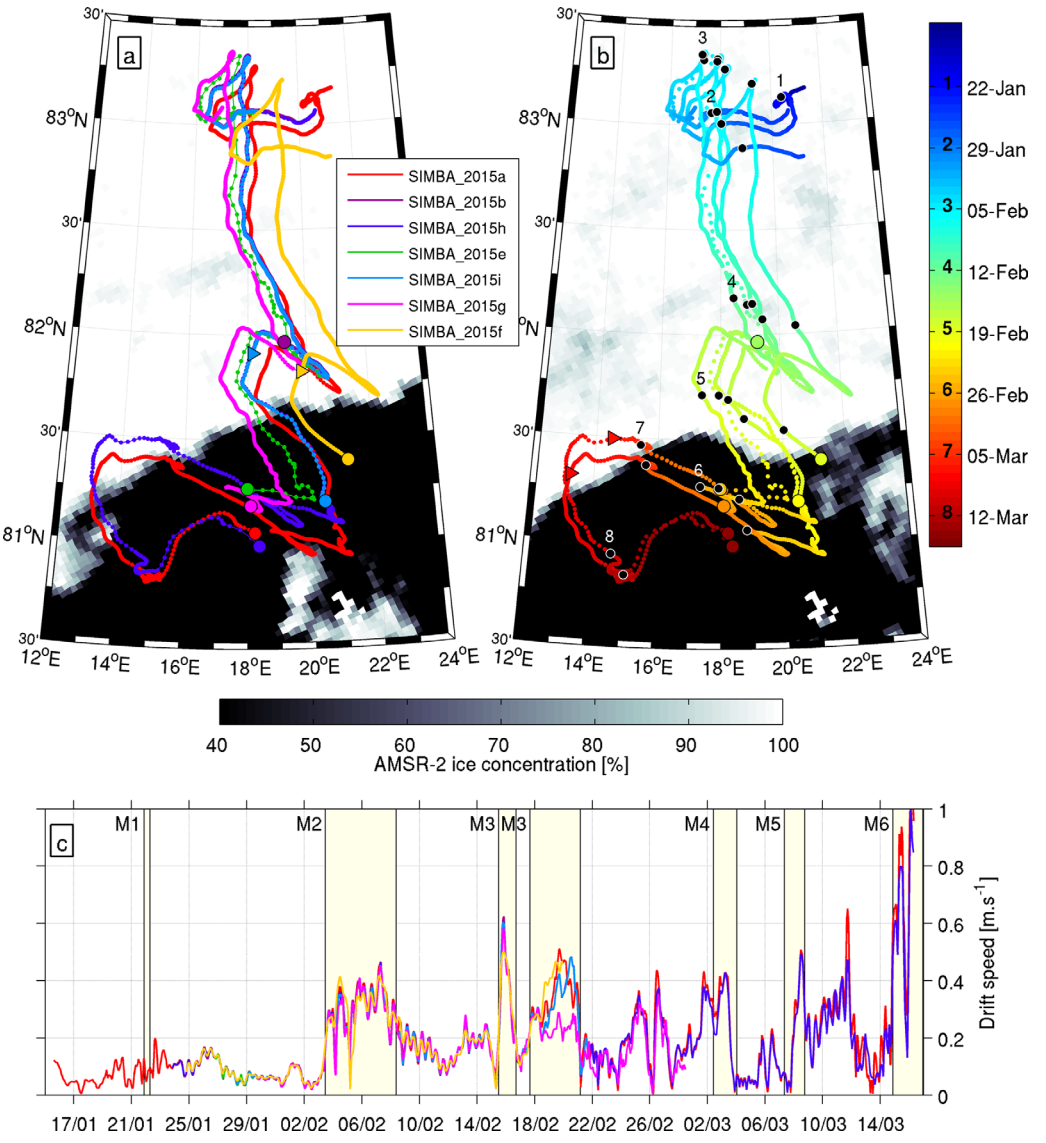

Figure 1. (a) Trajectories of the seven SIMBAs deployed in January–February of the N-ICE2015 campaign. Triangles indicate onset of the first snow-ice formation (SIF) event. Circles indicate the location of end of SIMBA record. Background is AMSR-2 ice concentration (%) on 17 February, the date of the first SIF event. (AMSR-2, advanced microwave scanning radiometer daily product on a 0.25° × 0.25° grid.) (b) Time along trajectories. Digits are used as points of reference (see colorbar). Background is AMSR-2 ice concentration (%) on 9 March, the date of the second SIF event. Triangles indicate onset of the second SIF event and circles are as in Figure 1a. (c) SIMBA drift velocities (m s^{-1}). Major storms are labeled M1, M2, . . ., M6 as described in *Cohen et al.* [2017].

8 March (see section 3). It is worth noting that the diffusivity proxy is not accurate enough to distinguish between slush and snow-ice. This will be further discussed in section 3.5.

2.2.3. Ice/Ocean Interface

Since the winter sea-ice remains colder than the ocean, the sea-ice/ocean interface can be estimated from temperature profiles alone. The ocean just below the ice is at or just above the freezing temperature (estimated from a near surface conductivity-temperature-depth (CTD) sensor see *Koenig et al.* [2016]). The first sensor of the SIMBA chain in the ocean was determined as the first sensor, downward of the snow/ice interface, with a temperature above the ocean freezing temperature. The location of the last sensor in the ice was determined as the sensor with a temperature that was below the mean ocean temperature by at least twice the ocean temperature standard deviation in that profile. Finally, the ice/ocean interface is defined as half way between the last sensor in the ice and the first sensor in the ocean. It can typically be estimated with 2 cm accuracy. This interface estimate is consistent with

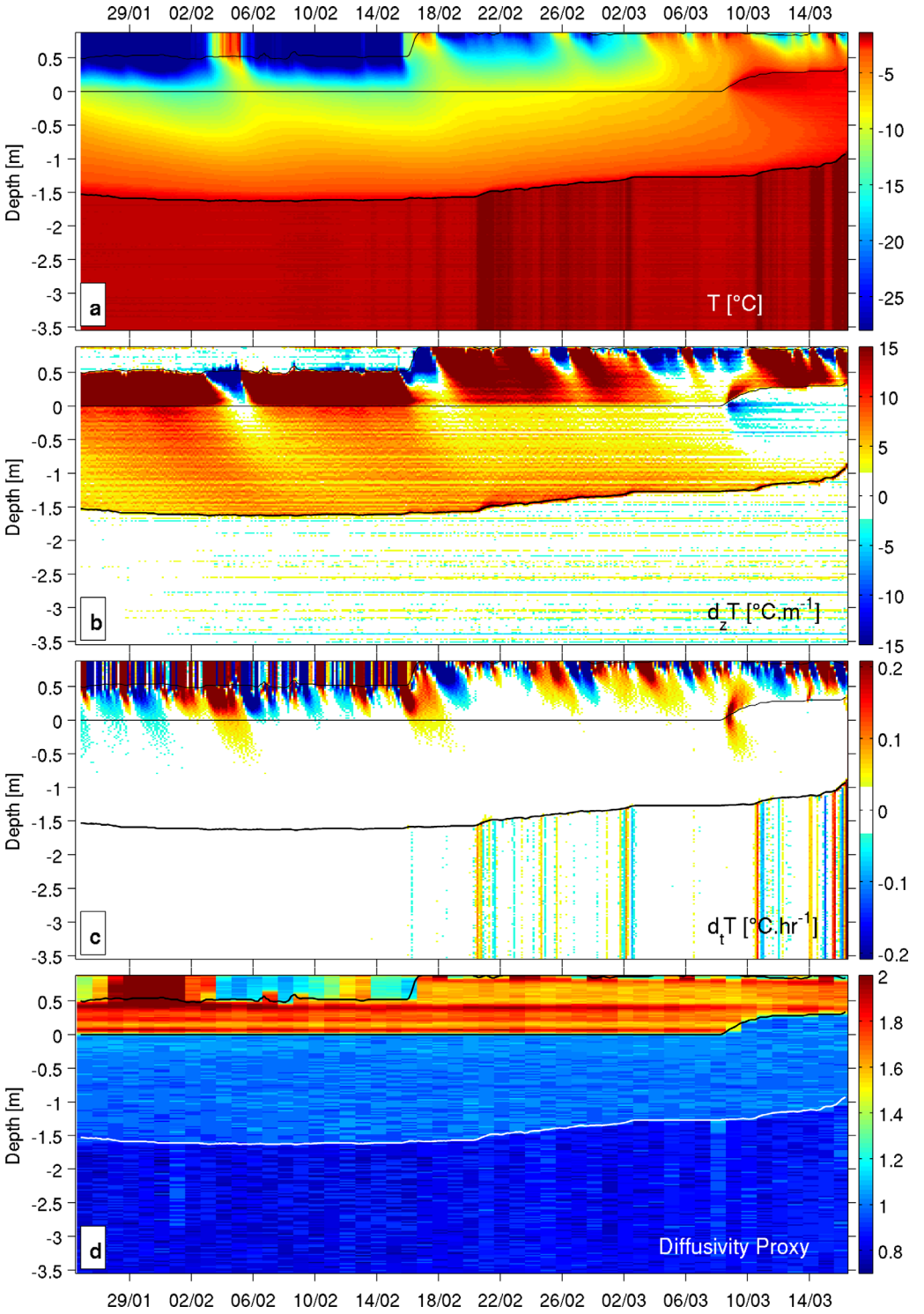

Figure 2. Data from SIMBA_2015h from top to bottom, (a) temperature (°C), (b) derivative of temperature with respect to the vertical (°C m^{-1}), (c) derivative of temperature with respect to time (°C h^{-1}), and (d) diffusivity proxy (no units) obtained from the heating mode. *y* axis is vertical distance (m) referenced to the initial ice-snow interface. Vertical resolution is 2 cm on all plots. Time resolution is 3 h on the 3 top figures and 24 h for diffusivity proxy. Isolines (24 h running mean) correspond to the air/snow, snow/ice, and ice/ocean interfaces derived as explained in section 2. Color scale in panel a is nonlinear in order to show temperature changes in the ocean.

the thermal diffusivity proxy (Figure 2d) and the vertical and temporal derivatives of temperature (Figures 2b and 2c) and features basal melt events after 20 February corresponding to temperature changes in the ocean (Figure 2c).

2.3. One-Dimensional Ocean to Sea-Ice Flux Densities

In this section we present the calculations of the heat fluxes. We assume a horizontally homogeneous environment. The *z* axis is positive in the direction toward the sky and the heat from the ocean toward the ice is likewise positive. The examples are again from SIMBA_2015h. In the parameterization, when needed, the ice salinity is assumed to be 5 PSU and temperature in the ice is provided by the SIMBA.

2.3.1. Latent Heat Flux

We define the latent flux density as

$$F_l = \rho_{si} \frac{dh}{dt}$$

where ρ_{si} is the sea-ice density (900 kg m^{-3}), L is the latent heat of fusion of sea-ice (J kg^{-1}), and h is the sea-ice-ocean interface depth (m). Following *Bitz and Lipscomb* [1999], we estimate L = 0.89 L_0 where L_0 is the latent heat of fusion of pure ice. The latent flux is directly proportional to the change in time of the interface depth (Figure 3b). The uncertainty on the latent heat flux estimate assuming a 2 cm accuracy on h is 56 W m^{-2} for data with a 3 h resolution (101 W m^{-2} for data with 6 h resolution). The resulting latent heat flux values for SIMBA_2015h range from −100 to 400 W m^{-2}, while the basal melt events associated with ocean temperature increase stand out (Figures 3a and 3b).

2.3.2. Conductive Heat Flux

The classical formula for conductive heat flux F_c in the one-dimensional case reads

$$F_c = -k_{si} \frac{dT}{dz}$$

where k_{si}, the sea-ice thermal conductivity, is derived from equation k = 2.03 + 0.117 S/T [*Maykut and Untersteiner*, 1971] for S = 5 psu and T is the observed temperature from the SIMBA. The sea-ice thermal conductivity k varied between 1.8 and 1.9 W m^{-1} K^{-1} for SIMBA2015-h. These values are consistent with those measured and estimated in *Pringle et al.* [2006] for second-year ice (SYI). We estimated conductive fluxes every 2 cm and chose to show depths that were indicative of atmospheric influence 20 cm below ice-snow interface, ocean influence 6 cm above ice-ocean interface and two intermediate depths between those two levels (Figure 3c). Those precise values are not critical, the purpose is just to illustrate how atmospheric and ocean influence are felt through the ice. The vertical gradients at the three upper levels were estimated by linear interpolation around the position and the gradient at the lower level by second order polynomial regression over 12 sensors above the interface as profiles are less linear near the ice bottom when ocean temperature changes. Resulting conductive fluxes for SIMBA_2015h range between −7 and + 22 W m^{-2}. As expected, the conductive flux near the snow/ice interface (Figure 3c) has the largest amplitude variations and reflects atmospheric temperature changes with about 8 day lag at the beginning of the time series, between 25 January and 16 February, when snow is 42 cm thick. After 16 February, the 88 cm-thick snow cover insulates the ice from atmospheric fluctuations and the conductive flux remains below 10 W m^{-2} until 8 March when snow-ice formation occurs (section 3) and the conductive flux becomes negative. The conductive flux at 30 cm above the ice/ocean interface (Figure 3c) remains around 10 W m^{-2} except after the formation of snow-ice. The near bottom flux (Figure 3c) is positive during basal melt events following the ocean temperature peaks (Figure 3a) except after 8 March during snow-ice formation (section 3).

2.3.3. Sensible Heat Flux

The sensible heat flux in the ice between two levels distant by p sensors (2p cm) is given by

$$F_s(i) = \sum_{j=i}^{i+p} \rho_{si} C_{si} \frac{dT}{dt_j} \; Dz$$

where C_{si} is the effective specific heat of sea-ice as defined by *Ono* [1967] and Dz is the distance between 2 sensors (2 cm). The sum is computed between sensor i at level z1 and sensor i + p at level z1 + 2p. The sensible heat flux between 6 and 30 cm above the ice-ocean interface varies between −4 and +10 W m^{-2} (Figure 3d).

In principle the residual flux, computed as the sum of the conductive heat fluxes at 6 and 30 cm and the sensible heat flux between those two levels, ($F_{Re} = F_{C6cm} + F_{C30cm} + F_{S6\text{-}30}$), should be zero under the assumption of a horizontally homogeneous environment. The residual flux never exceeds 2.9 W m^{-2} (Figure 3e). The residual flux can be seen as the sum of the errors in the three fluxes. The accuracy on the sensible heat flux is estimated to be 2.3 W m^{-2} considering the accuracy of temperature measurements (0.1°C) as

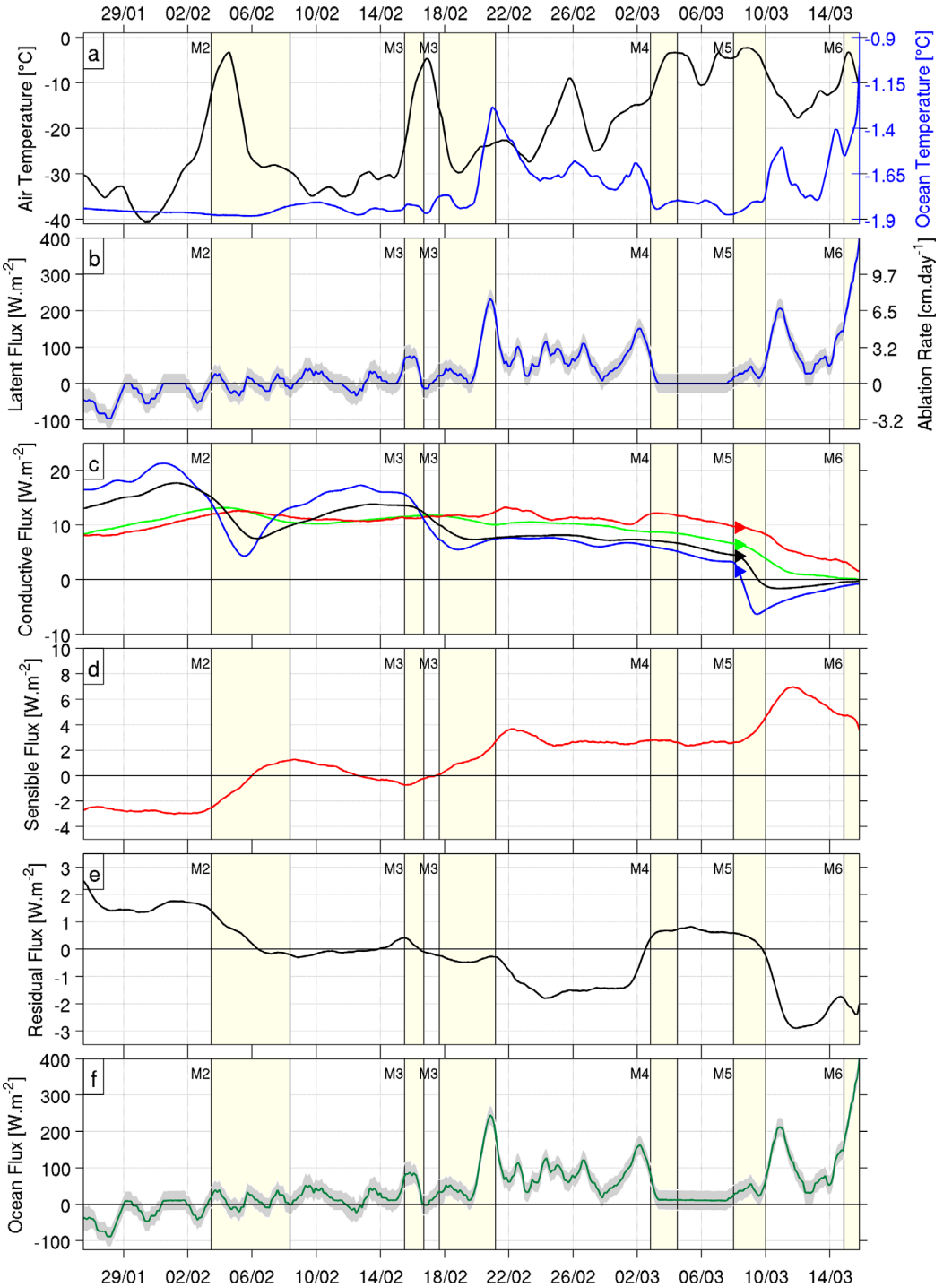

Figure 3. (a) Time series of air temperature from the weather station on the IAOOS (Ice Atmosphere Ocean Observing System) ice-tethered platform [*Koenig et al.*, 2016] hosting SIMBA_2015h (black line, left axis) and ocean temperature from SIMBA_2015h (mean of ocean temperatures, blue line, right axis); time series of heat flux densities (W m^{-2}) estimated from SIMBA_2015h. (b) Latent heat flux (left axis) and basal ablation rate (cm d^{-1}) (right axis), (c) conductive heat flux (blue: 20 cm below the snow-ice interface; black: 50 cm below the snow-ice interface; green: 30 cm above the ice-ocean interface; and red: 6 cm above the ice-ocean interface), (d) sensible heat flux between 30 and 6 cm above the ocean interface, (e) residual heat flux: sum of the conductive heat fluxes at 30 and 6 cm above the ice-ocean interface and the sensible heat flux between those two levels, and (f) ocean heat flux (latent heat flux plus conductive heat flux 6 cm above ice-ocean interface). All time series are smoothed with a 24 h running mean.

the sole source of uncertainty and taking a mean value for C_{si}. The accuracy for conductive fluxes can therefore be estimated to be less than 1 W m^{-2} and allows for confident use of the conductive flux calculated 6 cm above the interface in the following.

2.3.4. Ocean Heat Flux

The flux from the ocean to the ice can be derived as

$$F_{ocean} = F_l + F_c$$

F_l is the latent flux and F_c the conductive flux in the lower portion of the ice, here estimated 6 cm above the ice/ocean interface. As the latent heat flux is an order of magnitude larger than the conductive heat flux, the ocean heat flux is approximately equal to the latent heat flux (Figure 3f).

3. Evolution of the Snow and Ice Mass Balance

The methods described above were applied to the seven SIMBA records (Table 2, Figures 4 and 5) to retrieve the interfaces and compute heat fluxes. We first describe data and interfaces, then freeboard, and basal sea-ice melt, flooding and snow-ice formation. Basal ice melt is clear in all records after 15 February and flooding with snow-ice formation occurred at the end of the records of four SIMBAs (SIMBA_2015a, SIMBA_2015h, SIMBA_2015f, and SIMBA_2015i) (Figures 4 and 5). The seven SIMBAs were, at all times, located within a distance less than 50 km of each other (Figure 1).

3.1. Initial Conditions

In spite of their spatial proximity, the seven SIMBAs feature significantly different initial snow and ice thicknesses (Table 1). Initial snow thickness varied from 21 (SIMBA_2015e) to 55 cm (SIMBA_2015h) and initial ice thickness from 90 (SIMBA_2015f) to 158 cm (SIMBA_2015e). The average snow thickness in the region of the deployment site agrees well with the initial values of the SIMBAs (Table 1). During the winter months of the N-ICE 2015 camp, observed snow thicknesses, on average 33 ± 14 cm over first-year ice (FYI) and 52 ± 12 cm over second-year ice (SYI) [*Rösel et al.*, 2016], were larger than expected based on climatology (from 28 to 35 cm without distinction of ice type) [*Warren et al.*, 1999]. Note that snow was intentionally removed at SIMBA_2015e.

All freeboards were small (less than +4 cm) and even negative at two sites (–4 and −1 cm at SIMBA_2015i and SIMBA_2015f). Differences in initial conditions depend upon the local floe history prior to deployment (young, old, level or deformed ice, surface topography for snow deposition) and the location of the SIMBA on the floe. The age of the sea-ice on which the instruments were deployed varied from SYI to FYI (Table 1). Sea-ice cores were taken only for a number of the ice floes in the close vicinity of the research vessel and we can only establish with certainty that SIMBA_2015h and SIMBA_2015i were deployed on older sea-ice with a desalinated top part, while the ice at SIMBA_2015f had a typical salinity profile of FYI. The lower average amount of snow cover in the vicinity of the deployment site for SIMBA_2015b, SIMBA_2015e, and SIMBA_2015g might suggest that the floes would be FYI, although snow thickness is not a reliable metrics for distinguishing sea-ice age.

Table 2. Snow and Ice Thicknesses and Ice Freeboard: Initial Values, Values at the Onset, and After Snow-Ice Formation (SIF)[a]

	SIMBA_2015h	SIMBA_2015a	SIMBA_2015i	SIMBA_2015f	SIMBA_2015b	SIMBA_2015g	SIMBA_2015e
Snow-Ice Formation (SIF)							
SIF onset (DD/MM HH UTC)	8/03 8 A.M.	9/03 3 P.M.	17/02 7 P.M.	17/02 4 P.M.		No snow-ice observed	
SIF record length (h)	192	162	90	48			
Total Snow Thickness (cm)							
Initial	55	46	53	43	30	36	21/0
At SIF onset	90	50	85	55			
After SIF	55	35	43	37		No snow-ice observed	
Ice Thickness Budget (cm)							
Bottom ablation	71	71	15	2	9	20	8
Snow-ice	32	18	40	18			
Total change	−39	−53	25	16		No snow-ice observed	
Fraction of snow-ice (%)	27.6	22.8	27.8	17.0			
Estimated Freeboard (cm)							
Initial	2	2	−4	−1	4	2	2
At SIF onset	−12	−1	−12	−4			
After SIF	+0	+1	+3	+3		No snow-ice observed	

[a]Fraction of snow-ice thickness (%) to total ice thickness at the end of the records is also given.

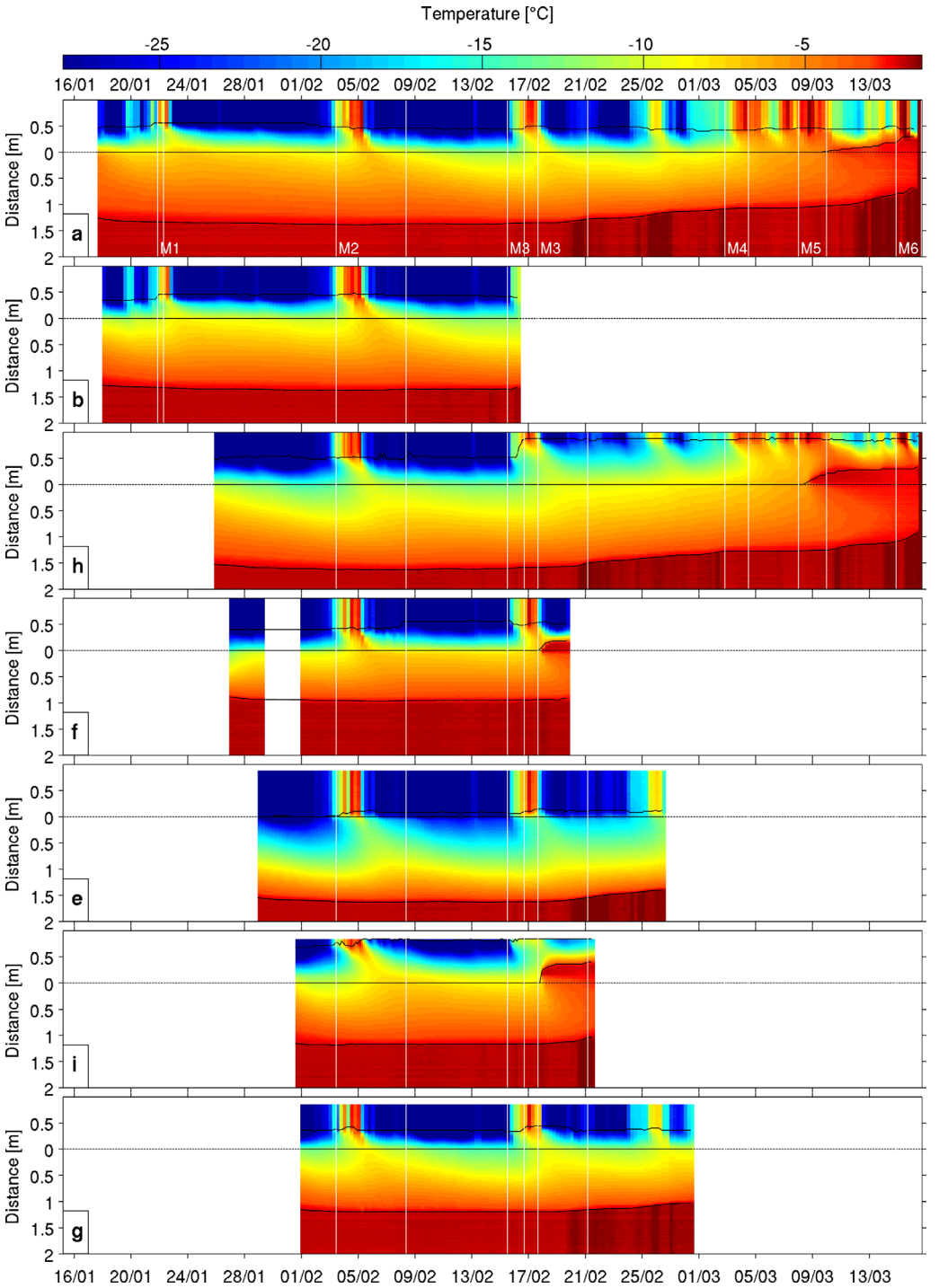

Figure 4. Temperature profiles (°C) and interfaces as a function of time for the seven SIMBAs. Color scale is nonlinear in order to show temperature changes in the ocean. Temporal resolution varies as indicated in Table 1 (3 h for SIMBA_2015i and SIMBA_2015h and 6 h for the others). *y* axis is vertical distance (m) referenced to the initial ice-snow interface. Vertical resolution is 2 cm. Black isolines (24 h running mean) correspond to the air/snow, snow/ice, and ice/ocean interfaces derived as explained in section 2.

3.2. Evolution of Temperature Profiles, Thermal Diffusivity Profiles, and Interfaces

All SIMBAs experienced similar atmospheric conditions as they were close to each other. In fact, the parts of the chain deployed through the air all show sudden temperature peaks associated with the storms and a gradual warming trend [*Hudson et al.*, 2016] through the observation period (Figure 4). Air temperatures

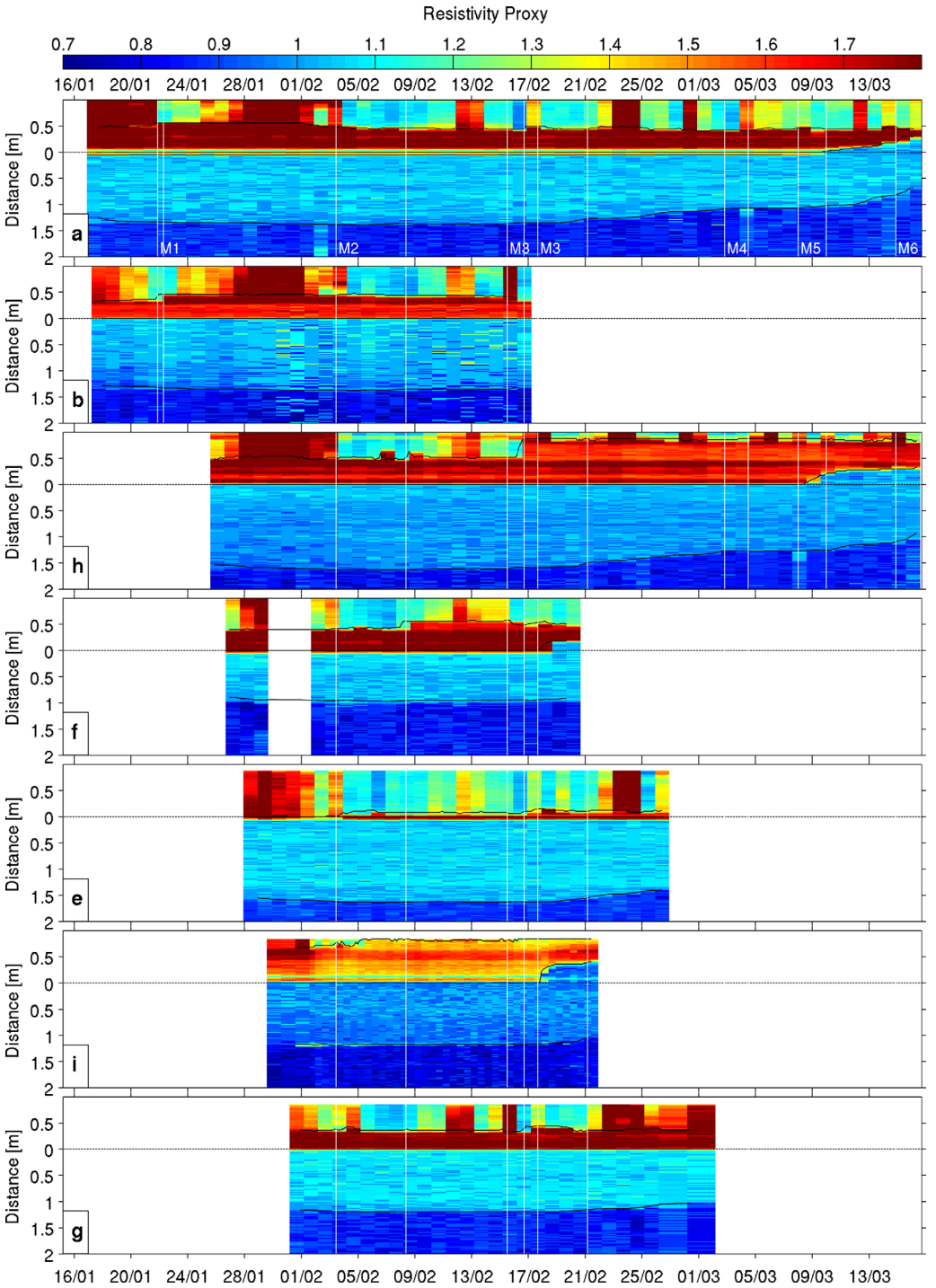

Figure 5. Thermal diffusivity proxy profiles and interfaces as a function of time for the seven SIMBAs. Time resolution varies as indicated in Table 1 (12 h for SIMBA_2015i and 24 h for the others). *y* axis is vertical distance (m) referenced to the initial ice-snow interface. Vertical resolution is 2 cm. Isolines (24 h running mean) correspond to the air/snow, snow/ice, and ice/ocean interfaces.

varied from −42 to 0°C. Note that the top of SIMBA_2015h chain was entirely covered by snow from 17 February onward (Figures 4 and 5) and the snow thickness was estimated to be 90 cm (Table 2).

Snow thickness, with initial values ranging from 21 cm (SIMBA2015-e intentionally artificially turned to 0 cm) to 55 cm (SIMBA2015-h), evolved only during storms and during flooding events leading to snow-ice formation (Figure 6a). The change in snow thickness observed during the storms varied greatly from one SIMBA to

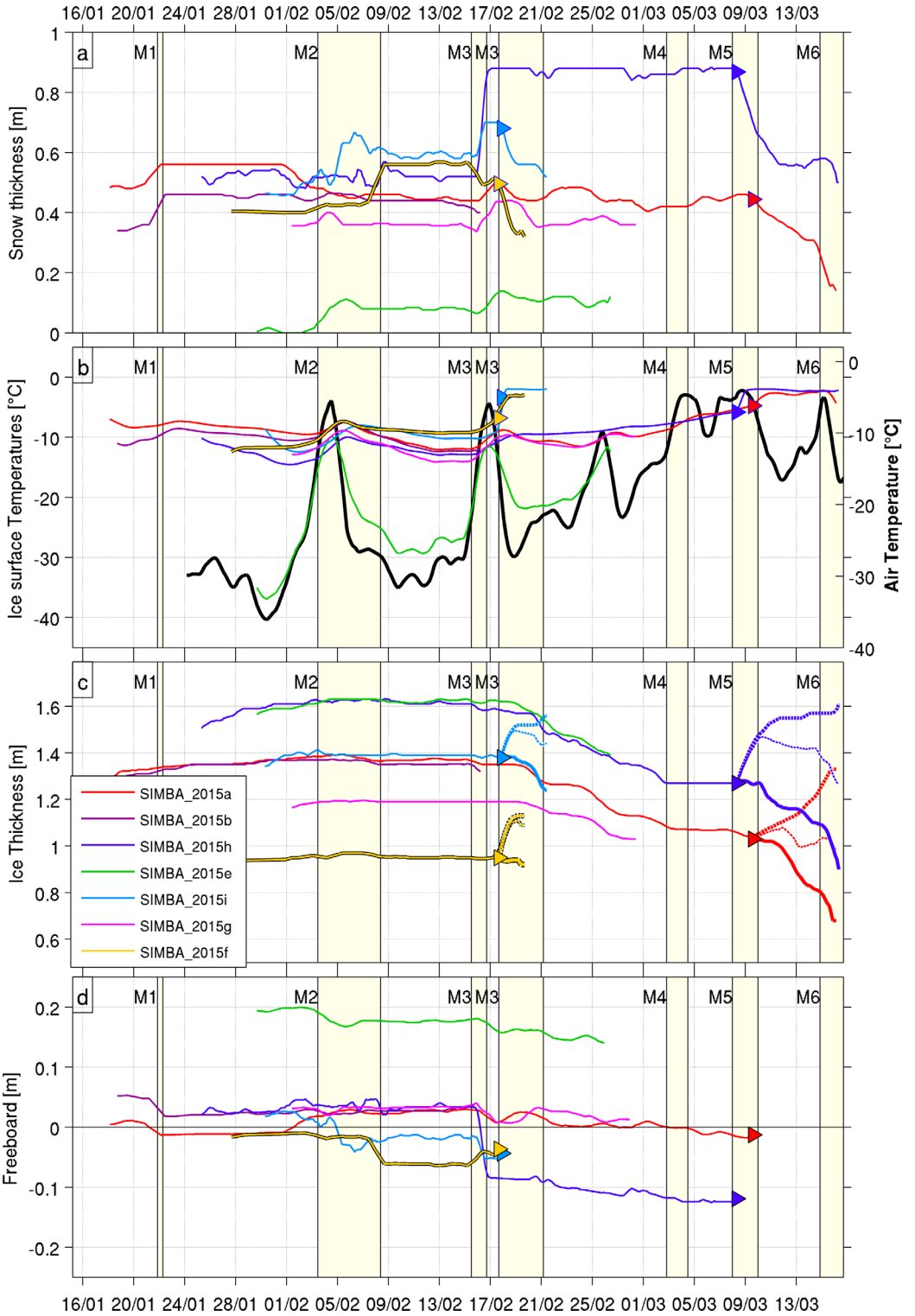

Figure 6. Times series of (a) snow thickness (m), (b) temperature (°C) at the snow-ice interface (color) and air temperature (black line), and (c) ice thickness (m). Note that when slush/snow-ice formation occurs, the ice thickness line separates into three branches: the bottom one (thick) indicates the ice thickness without taking the slush/snow-ice into account, the top one (thick) the ice thickness without taking into account basal melt, and the one in the middle (thin line) the ice thickness including slush/snow-ice, and (d) freeboard estimates (m). All time series are smoothed with a 24 h running mean. Color associated to each SIMBA is indicated in insert. Triangles indicate onset of snow-ice formation. Storm periods are indicated as in Figure 1c.

another, suggesting important differences in snow redistribution, accumulation or ablation, likely due to interaction of winds and snow transport with the surface topography of the floe, and possibly also local snow accumulation/erosion due to the SIMBA support structures. During M1, the only two active SIMBAs, SIMBA_2015a and SIMBA_2015b, recorded a 10 cm increase in snow depth. During M2, only three SIMBAs out of seven (SIMBA_2015e, i, and f) showed significant snow accumulation (10, 25, and 15 cm, respectively) which did not occur on the same day. Three others (SIMBA_2015b, h, and g) did not show any change while SIMBA_2015a showed a decrease of 15 cm. During M3, SIMBA_2015h experienced 45 cm of snow accumulation whereas SIMBA_2015f and SIMBA_2015i experienced significant drops of 20 and 30 cm in snow thickness, respectively, because of flooding (Figure 6a). Thereafter, snow thicknesses did not change much until flooding after M5 (40 cm decrease for SIMBA_2015h and 30 cm for SIMBA_2015a). Note that SIMBA_2015e (green line in Figure 6), which was intentionally left with bare ice, retrieved 17 cm of snow.

The insulating effect of the snow layer can be readily appreciated when comparing temperatures at the ice-snow interface to air temperatures (Figure 6b). The air temperature range exceeds 40°C, whereas temperature at the snow-ice interface remain around −10°C (±5°C) except in the case of SIMBA_2015e where temperature at the top of the ice followed air temperature as the snow cover was nonexistent or very thin (Figure 6b). The snow cover provides thermal insulation from air temperature, regulates temperature fluxes, and affects the thermal evolution of sea-ice [*Massom et al.*, 2001].

During M3, when Floe 1 of the N-ICE2015 campaign broke up, two SIMBAs (SIMBA_2015b and SIMBA-2015f) stopped working. All the other SIMBAs documented significant ice ablation at the bottom (Figure 6c). Basal ice melt started around 18 February, when the distance to the open water was 45 km and went on until the end of the time series, with a pause between M4 and M5. By 15 March, when the distance to the open water was just 2 km, total ice ablation was about 68 cm at the two remaining SIMBAs (SIMBA_2015a and SIMBA_2015h) (Table 2). This is discussed further in section 3.4.

Four SIMBAs displayed a typical signal for a flooding above the initial ice/snow interface (SIMBA_2015f and SIMBA_2015i around 17 February, SIMBA_2015a and SIMBA_2015h around 8 March, Figures 4 and 5). The flooding heats the base of the snow, which in turn heats the surrounding snow and ice. The thermal diffusivity proxy (Figure 5) readily turns from snow values to values typical of ice. Slush is formed. The flooding events leading to slush and subsequent transformation of slush into snow-ice are further examined in section 3.5.

3.3. Freeboards

The sea-ice thickness and snow depth time series were used to estimate the freeboard development for each SIMBA using Archimedes buoyancy principle, that is a vertical buoyancy balance where a mass per unit volume of sea water supports sea-ice and snow. The freeboard h_f is given by

$$h_f = h_i - \frac{\rho_i h_i + \rho_s h_s}{\rho_w}$$

where h_i is the ice thickness, h_s the snow thickness, ρ_w the density of seawater, ρ_s the density of snow, and ρ_i the density of sea-ice. Typical density values (1028 kg m^{-3} for ρ_w, 330 kg m^{-3} for ρ_s, and 900 kg m^{-3} for ρ_i) provided reasonable estimates of the freeboard (Figure 6d). The initial estimated freeboard values are of the same sign and magnitude (within 2 cm) as the observed initial conditions, except in the case of SIMBA_2015e. At this buoy, the original snow cover depth was not restored after the deployment and while the initial estimated freeboard is about +18 cm (in green in Figure 6d), the observed initial freeboard is only +2cm (Table 1). If we replace the snow depth measured by the SIMBA chain by the average snow depth measured in the vicinity of the buoy (Table 1), the calculated freeboard agrees with the observed initial freeboard. The estimated freeboards tend to decrease with time as snow accumulates (Figures 6a and 6d). The decrease in estimated freeboard varies with snow accumulation and is largest for SIMBA_2015h (Figure 6d). The four SIMBAs with a positive estimated freeboard right before the floe broke up (SIMBA_2015a, b, e, and g) did not observe flooding (slush formation, Table 2), while SIMBA_2015f and SIMBA_2015i with negative estimated freeboards of −10 cm at the time of M3, showed flooding. Slush formation reduced the snow thickness (–20 cm at SIMBA_2015f and −40 cm at SIMBA_2015i, Figure 6a), increased the ice thickness (by 20 and 40 cm, respectively, including thickness of the slush layer, Figure 6c). SIMBA_2015h has a similar estimated negative freeboard (–10 cm) but did not show slush formation at the

end of storm M3. This suggests that SIMBA_2015h was on a floe that did not break up or that the snow accumulated very locally around the SIMBA chain. Note that until storm M3 ice thickness changes are small, and that freeboard changes are due to snow accumulation. Basal melt starts after storm M3. After storm M3, the ice thickness diminished (Figure 6c) while snow thickness was unchanged and freeboard decreased further for SIMBA_2015a and SIMBA_2015h (Figures 6a, 6c, and 6d). During storm M5, flooding occurred with a slush layer of 30 cm at SIMBA_2015h and 25 cm at SIMBA_2015a (see Table 2).

The flooding events on 19 February (two SIMBAs during storm M2) and on 8 March onward (two SIMBAs after and during intense basal ice melt) and subsequent refreezing of slush into snow-ice are examined in more detail in section 3.5.

3.4. Heat Fluxes and Basal Melt

Conductive heat flux densities in the ice estimated at the interface with snow range from 90 to -50 W m^{-2} (Figure 7a). They vary with atmospheric temperatures (Figure 6b): they are in phase for SIMBA_2015e (not shown), the location with no or little snow cover, and with some delay for the others. Negative values are observed at SIMBA_2015e during storms when the air temperatures peak (not shown) and at the four SIMBAs that experienced flooding at the interface with the warm slush. These conductive fluxes away from the slush are used to estimate how much slush solidifies into snow-ice in section 3.5.

All conductive heat flux densities estimated 6 cm above the ice/ocean interface are in the range 5–32 W m^{-2} (Figure 7b). Until 15 February, while the ocean is at the freezing temperature (Figure 7e), they vary with atmospheric temperatures with some delay (Figure 6b). After this date, they reflect ocean temperature changes and temperature changes due to flooding and snow-ice formation.

Latent heat flux densities, which are proportional to ablation rates, (Figure 7c) feature values larger than 100 W m^{-2} several times after 15 February. The bottom melt common to all SIMBAs occurs in rather short, sporadic events associated with warm ocean temperature pulses (Figure 7e). High melting rates ($>$6 cm d^{-1}), such as reported in *Sirevaag* [2009] in the same area, are observed. Values of latent heat flux densities as large as 400 W m^{-2} are found at the end of the time series. The negative values at the beginning of all latent flux density time-series (during 2–3 days) result from the refreezing of the drilled hole (2 in. diameter) through which the SIMBA string was deployed. They are not only driven by vertical fluxes but also horizontal conduction in the ice.

Ocean heat fluxes estimated as the sum of the conductive flux 6 cm above the sea-ice-ocean interface and the latent heat flux associated with ice melting mimic the latent heat fluxes which are an order of magnitude larger than the conductive fluxes (Figure 7d). These large ocean fluxes, with peak values of 400 W m^{-2}, are associated with warmer ocean temperatures when the ice floes drifted on top of shallow Atlantic waters north of Svalbard [*Koenig et al*., 2016]. The mean ocean-to-ice heat flux over the Svalbard continental slope was 150 W m^{-2} leading to a basal ice melt of 60 cm in less than 15 days. *Koenig et al*. [2016] showed that the sea-ice melt events were associated with near 12 h fluctuations in the upper ocean temperature and salinity corresponding to the periodicity of tides and near-inertial waves potentially generated by winter storms. These values are comparable to ice-ocean heat fluxes estimated in the same region in April 2003 (values peaking at 600 W m^{-2}) [*Sirevaag*, 2009] or estimated over the Yermak Plateau in February 2003 (values peaked at 100 W m^{-2}) [*McPhee et al*., 2003].

3.5. Flooding and Snow-Ice Formation

Flooding and slush formation were readily seen on the diffusivity proxy (Figures 4 and 5) and on the temperature itself (Figures 4 and 5). Indeed, the flooding has a strong temperature signature with initial warming at the ice-snow interface and subsequent heat propagation throughout the snow and ice system (Figures 4 and 5). At flooding, the diffusivity proxy values drop to ice-like values (Figure 5). Snow flooded by salty water, through either vertical infiltration through brine channels or lateral infiltration from seawater, forms a warm layer of slush (Figures 8a and 8b). Then the slush progressively solidifies into snow-ice as latent heat flux of snow-ice formation is converted into conductive heat fluxes in the snow above and ice below [*Eicken et al*., 1994]. The diffusivity proxy values do not allow distinguishing between slush and snow-ice (Figure 8b).

The temperature changes associated with the flooding are best observed in the time derivatives of temperature which peaks at 2.4°C/h (Figure 8c). Then, there is progressive freezing into snow-ice as latent heat

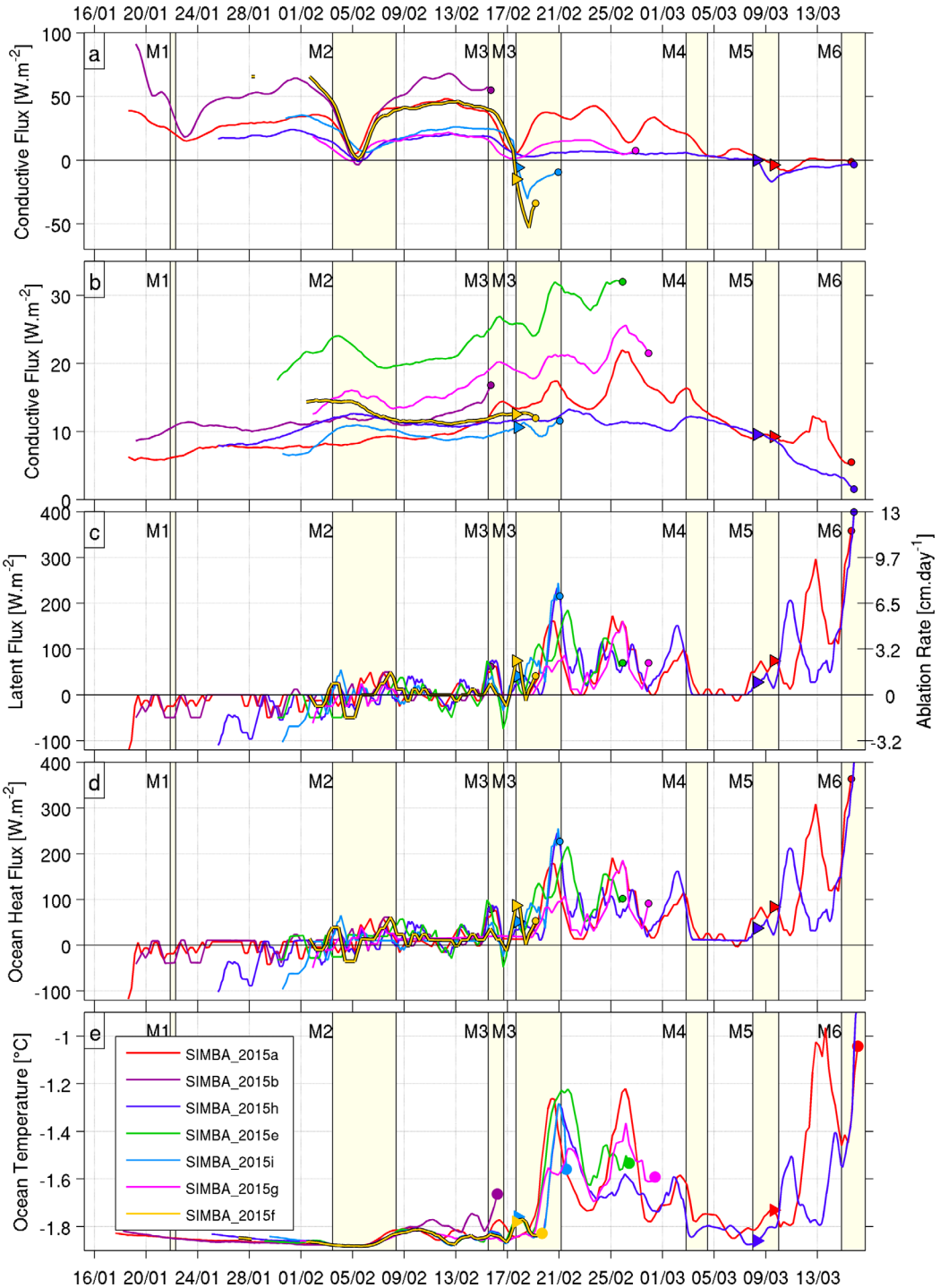

Figure 7. SIMBA time series of (a) conductive heat flux densities in the ice at the snow-ice interface (W m^{-2}) (SIMBA-2015e provides larger values), (b) conductive heat flux densities 6 cm above the ice-ocean interface (W m^{-2}), (c) latent heat flux densities at the ice-ocean interface (W m^{-2} left axis) and equivalent ablation rate (right axis in cm d^{-1}), (d) ocean heat flux densities (W m^{-2}), and (e) ocean temperature (°C) (mean of observations in the ocean). All time series are smoothed with a 24 h running mean. Color code corresponds to the different IMBs as indicated. Triangles indicate onset of snow-ice formation. Storm periods are indicated as in Figure 1c.

from solidifying ice is expelled from the flooded snow layer through conductive fluxes in the snow above and ice below (Figure 8d). Assuming that the mass fractions of snow and water in snow-ice are 2/3 and 1/3, respectively [*Eicken et al.*, 1995; *Kirillov et al.*, 2015], the thickness of slush that turns into snow-ice at each time t can be estimated as

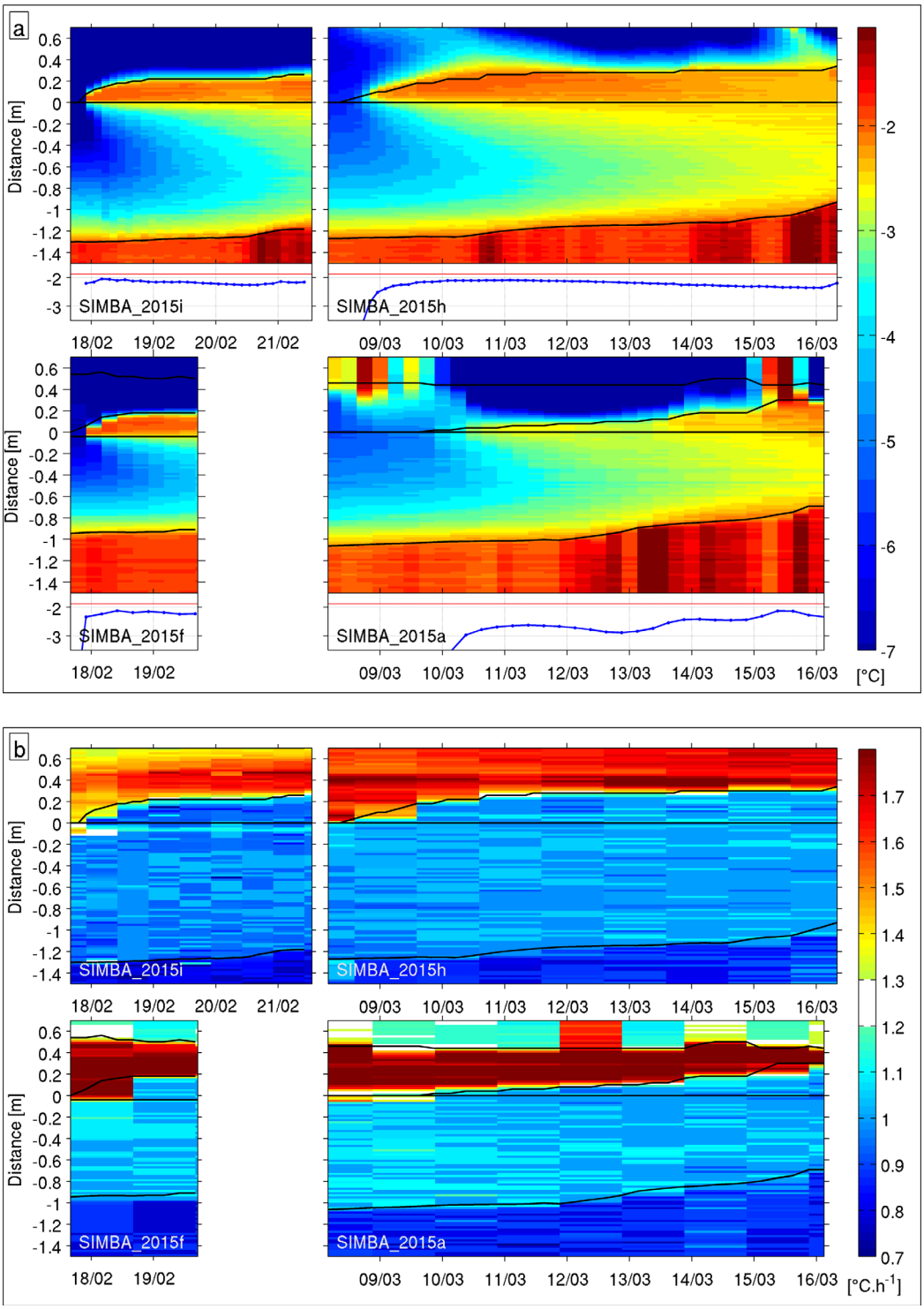

Figure 8. (a) Close-up of temperature profiles (°C) during periods of flooding and snow-ice formation (SIMBA_2015i, SIMBA_2015h, SIMBA_2015f, SIMBA_2015a). Temperature scale is nonlinear. The blue curve below corresponds to the average temperature values between real time and initial snow/ice interface. Red line is ocean freezing temperature. (b) Close-up of diffusivity proxy profiles (°C) during periods of slush/snow-ice formation (SIMBA_2015i, SIMBA_2015h, SIMBA_2015f, SIMBA_2015a). (c) Close-up of the profiles of the time derivative of temperature (°C h^{-1}) in the course of slush/snow-ice formation (SIMBA_2015i, SIMBA_2015h, SIMBA_2015f, SIMBA_2015a). (d) Close-up of the profiles of the vertical derivative of temperature (°C m^{-1}) in the course of slush/snow-ice formation (SIMBA_2015i, SIMBA_2015h, SIMBA_2015f, SIMBA_2015a). The black curve below corresponds to the flooded snow thickness, the blue (red) curve to the part that solidified into snow-ice due to conductive fluxes through the ice (ice and snow). *y* axis is vertical distance (m) referenced to the initial ice-snow interface. Vertical resolution is 2 cm. Black isolines from top to bottom represent air/snow interface, initial snow/ice interface, and ice/ocean interface. Green isolines represent snow/ice interface evolution.

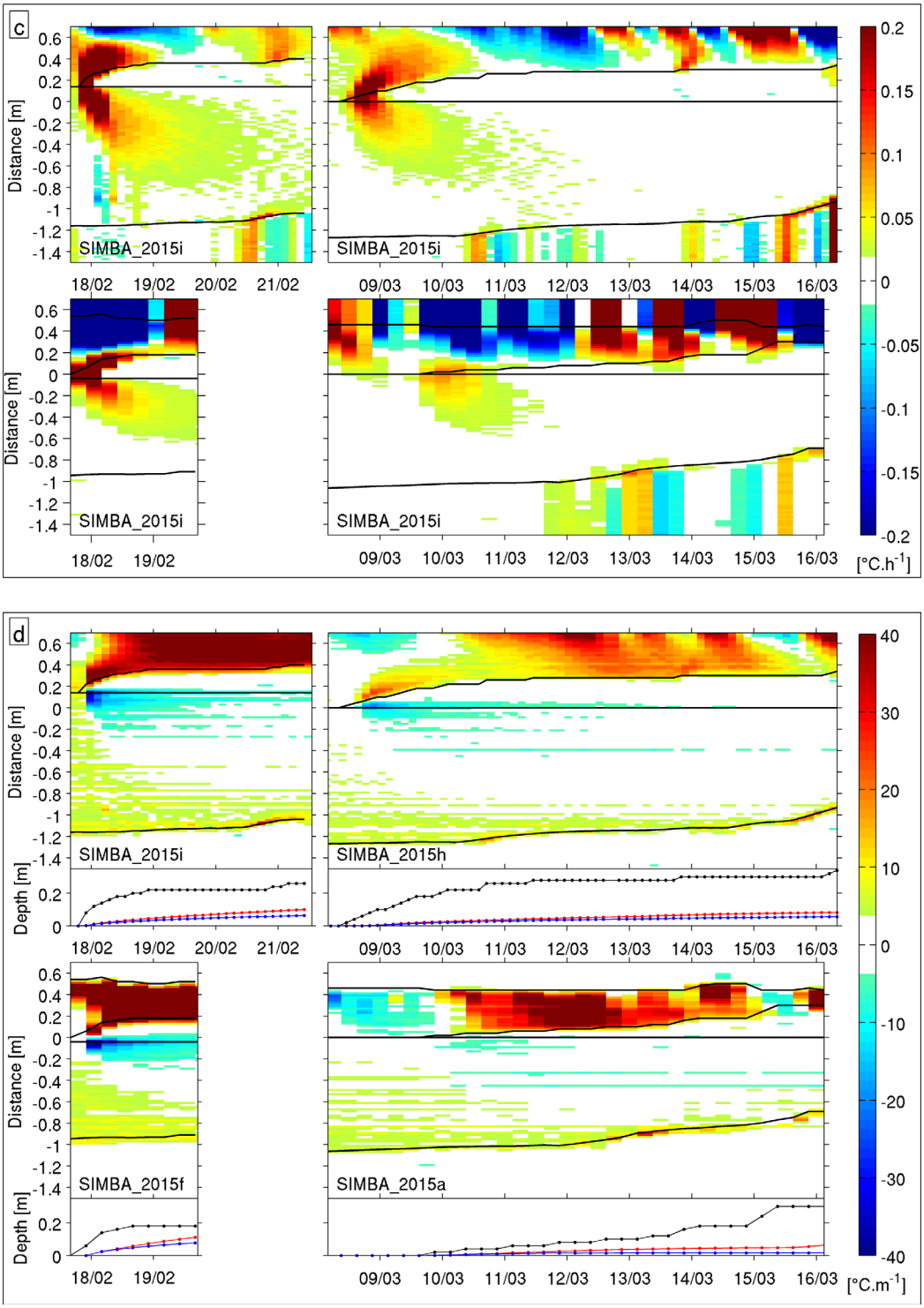

Figure 8. (continued).

$$h(t)=\frac{3(F_S(t)+F_i(t))}{\rho L}$$

where $F_s(t)$ and $F_i(t)$ are the conductive heat flux densities in the snow and in the ice at the flooded layer interface at time t, ρ is the ice density (taken as 900), and L the latent heat of fusion. These conductive flux

densities (F = –k dT/dz) are calculated with k ≅ 0.3 W m^{-1} K^{-1} at the base of the snow [*Yen*, 1981] and k in the ice as in section 2.3.2. The snow-ice layer thickness H(t) is then estimated as

$$\int_{t_0}^{t} h(s)\ ds$$

with the time integration running from the time of the flooding t_0 until time t (Figure 8d). This rough calculation, which neglects any lateral flux, gives an order of magnitude of about 10 cm of snow-ice at the end of the four records (Figure 8d).

During the first flooding event (17 February, SIMBA_2015i and SIMBA_2015f), the temperature of the new slush layer right after flooding was close to the ocean freezing point (Figure 8a). In 3 h, 25 and 10 cm of slush was formed at SIMBA_2015i and SIMBA-2015f, respectively. The initial temperature at the snow/ice interface before flooding was about −8.5°C and the 3 h resolution record at SIMBA_2015i indicates that the ocean freezing temperature of about −2°C was reached in less than 3 h (blue line in Figure 8a). The heat release associated with the flooding on 18 February propagated through the ice and increased the ice temperature by about 3°C down to 70 cm depth (Figures 8a and 8b). The 4 day long record at SIMBA_2015i shows that the flooded layer temperature decreases slightly (blue line in Figure 8a) and then increases again to ocean freezing temperature as further flooding takes place on 21 February (5 cm) as corroborated by another subsurface peak in the time derivative of temperature (Figure 8a). The amplitude of the peak in time derivative is smaller as the ice was warmer and closer to ocean freezing temperature (Figure 8c). This second period of flooding follows 5 cm of basal melt (Figure 8a), suggesting freeboard adjustment to changed ice thickness. Estimates of the conductive fluxes suggest a latent heat change within the flooded layer sufficient to freeze the equivalent of 10 cm of snow-ice in 3 days, or the equivalent of half the total slush layer thickness. The short 2 day record of flooding and subsequent snow-ice formation for SIMBA_2015f provides information that are consistent with SIMBA_2015i: a rapid flooding with a strong heat release, underlying ice warming by 3°C over 50 cm depth (Figures 8a and 8b), progressive snow-ice formation of about 11 cm in 2 days estimated from the heat release by conductive fluxes (Figure 8d). Conductive fluxes through the snow at the flooded layer interface at SIMBA-2015f were larger than at SIMBA_2015i as the remaining snow layer above the flooded layer was thinner (35 versus 55 cm). In both cases, although air temperatures fell below −20°C after the storm M3, the remaining snow layer damped heat exchanges with the slush layer and conductive fluxes through the ice, although the ice had been heated up by the flooding, had a larger contribution to the solidification of the slush than conductive fluxes through the snow (Figure 8d).

The second major flooding event occur later in March and further south at a time when ice temperature at the surface was −4°C (SIMBA_2015h on 9 March and SIMBA_2015a on 10 March and onward) (Figure 8a).

Flooding at SIMBA_2015h, documented with a 3 h time resolution, is gradual as a 20 cm-thick slush layer is formed in 2 days. Slush temperature right after flooding is also near ocean freezing temperature (blue line in Figure 8a). The temperature of the flooded layer then decreases slowly as it is cooled from above and below. A second flooding event at SIMBA-2015h is detected on 13 March, with 5 cm more of flooding and a small heat release (Figures 8a and 8c). Conductive flux densities at the flooded layer interface are smaller than during the February flooding event as ice and snow temperatures are larger than in February and about 8 cm of slush solidified into snow-ice in 7.5 days (Figure 8d).

The flooding event on 10 March at SIMBA_2015a is rather different than the one just described. The amount of slush formation at SIMBA_2015a on 10 March is small and increases gradually, with a few cm on 13 March and 5 cm on 15 March. The temperature of the slush is colder (–3°C) at formation until 14 March and it increases to ocean freezing temperature on 15 March (Figure 8a). Slush formation occurs at a time when the sea-ice, only 1 m thick, has been warmed up from below and above: the ice temperature on 9 March, right before slush formation, ranges between −2 and −4.7°C from bottom to top. The ice is probably more permeable [*Golden et al.*, 1998] and the cold temperature of the slush formed (–3°C), well below ocean freezing temperature, could be a sign of a process including vertical infiltration of brines rather than just lateral infiltration of seawater. However, the temperature pulse at flooding is at the base of the snow

suggesting that flooding was from seawater intrusion (or brine that percolated up nearby and spread horizontally at the ice surface). Alternatively, the colder temperature of the slush could be due to the slow rate of intrusion, and the water was cooled as it flooded. Temperature pulses on 13 and 15 March at the base of the snow layer (Figure 8c) correspond to ocean temperature (–1.88°C) (Figure 8a) and further lateral flooding (5 cm on 13 March and 10 cm on 15 March) due to further freeboard adjustment as basal melt is active (25 cm of sea-ice melted between 12 and 16 March) (Figure 8). About 6 cm of slush solidified into snow-ice.

In all cases, the records after flooding are short (from 2 to 7 days) and stop before the whole slush layer solidified. The estimates of solidified snow-ice were produced assuming that the slush was made of 2/3 snow and 1/3 of water. If the initial snow was less dense and slush made of half water and half snow, the thickness of solidified snow-ice would be reduced by one third. The ratio of the slush thickness to the total ice thickness ranged between 17 and 28%.

4. Summary and Discussion

Seven SIMBAs, within a distance of 50 km from each other, continuously recorded snow and ice conditions in the Arctic Ocean north of Svalbard in the midwinter (January–March) 2015. The SIMBAs repeatedly observed temperature and thermal diffusivity proxy profiles with a 2 cm vertical resolution in air, snow, ice, and ocean below, allowing precise determination of interfaces and estimates of heat fluxes. They recorded temperature and snow depth changes associated with the six distinct synoptic events. Snow depths ranged from 30 to 90 cm and ice thicknesses from 0.9 to 1.6 m. The SIMBAs registered intense basal sea-ice melt when drifting over warm Atlantic waters north of Svalbard and ocean-to-ice fluxes peaked at 400 W m^{-2}. Four SIMBAs documented flooding and snow-ice formation. These are the first direct observations of snow-ice formation in the high Arctic. Flooding is evident from the simultaneous change in thermal diffusivity proxy (from high snow values to lower slush values), temperature increase and heat propagation throughout the snow and ice. Subsequent freezing of slush into snow-ice was estimated from the conductive fluxes into the snow above and ice below. The freezing was progressive and the records ended before the whole slush layer froze into snow-ice.

Two major flooding events were observed, one occurring after storm-induced floe break up, the other after intense basal sea-ice melt. The first flooding event (17 February) occurred at about 45 km from the open water (Figure 1a), preceded the basal melt onset and was associated to a major storm (M3) that lasted from 15 to 21 February [*Cohen et al.*, 2017]. In the vicinity of R/V Lance, cracks appeared on 16 February gradually breaking the floe into pieces less than 100 × 100 m large. On 17 February in the morning, we revisited SIMBA_2015f, while the base of snow cover was not flooded. SIMBA_2015f and SIMBA_2015i both detected flooding in the evening, while numerous cracks were visible from R/V Lance. From this moment on, revisits were no longer possible. Most probably, cracks allowed the ocean water to flood the floe surfaces. The ice before snow-ice formation was cold (profile temperature between −2 and −15°C) and impermeable. Most likely the snow-ice interface was forced down below sea level by the thick snow layer. Indeed, the consolidated ridges at the floe edges prevented lateral infiltration of seawater until the break up after which the snow was flooded and converted to slush at about the ocean freezing temperature. A layer of 25 cm of slush was formed in less than 3 h (time resolution of the instrument). The heat associated with the flooding increased the underlying ice temperatures by about 3°C. Then further heat was released into the snow above and the ice below as the slush layer progressively solidified. During the storm, the air temperatures rose above the freezing point (Figure 6b) and prevented the cracks and ridges to consolidate, but they dropped abruptly below −20°C by 18 February and facilitated the heat loss to the atmosphere (Figure 8d). However, the remaining snow after the flooding insulated the slush layer from the cold atmosphere and the contribution of the conductive fluxes through the snow to the freezing of the slush was smaller than that of the conductive fluxes through the ice. About 10 cm of slush solidified into snow-ice in 2–4 days (Figure 8d).

The second flooding event occurred during periods of intense basal melt, near the ice edge (about 15 km from the open ocean, Figure 1b), due to warm ocean temperatures (9–15 March). Flooding was gradual (a few days) and followed basal ice ablation. The ice before flooding showed temperatures above −4.5°C and it was likely permeable [*Golden et al.*, 1998]. The heat released by the flooding contributed to warm the ice from above (+3°C). Further lateral flooding at the ocean temperature (–1.88°C) was observed

simultaneously on the two SIMBAs (5 cm on 13 March and 10 cm on 15 March) due to further freeboard adjustment due to intense basal melt (25 cm of sea-ice melted between 12 and 16 March) (Figure 8). Conductive fluxes from the slush layer to the snow and ice layers were smaller than in February as the snow and ice were warmer and the slush layer colder. The estimated thickness of snow-ice formed (about 6–8 cm) was smaller than in February, although the records were longer (7 days versus 2 or 4).

In the Antarctic, flooding of the snow base is widespread because sea-ice thickness is small and snow fall abundant. Because of this, snow/ice interface is often pushed below sea level, hydraulically forcing the infiltration of brines (vertically) or seawater (laterally) into snow forming snow-ice [*Eicken et al*., 1994]. The contribution of snow-ice to the total ice mass in the Arctic has not received much attention so far. This is due to the fact that snow-ice has not been expected to form in the Arctic since the ratio of snow thickness to ice thickness being usually low [*Vihma et al*., 2014].

Here the snow-ice records are quite short, 7 days for the longest one (SIMBA_2015h), as the SIMBAs stopped recording soon after flooding either because they were recovered (SIMBA_2015h and SIMBA_2015i) or damaged. This could imply that the ice floes with snow-ice rapidly deteriorated over warm water and were a transient feature, and that the flooding accelerated the decline of the ice cover by warming the ice, thus accelerating the basal melt, and also mechanically weakening the ice cover. However, the particular event of flooding and subsequent snow-ice formation caused by floe break up and lateral flooding (opposed to the snow-ice formation caused by basal melt) may imply that in the future Arctic Ocean with possibly more abundant snow precipitation [*Overland et al*., 2012; *Bintanja and Selten*, 2014], generally thinner [*Maslanik et al*., 2007; *Lindsay and Schweiger*, 2015] and weaker sea-ice, more storms penetrating to high latitudes [*Graham et al*., 2017] and consequently higher deformation rates [*Itkin, et al*., 2017], we might expect more snow-ice formation that is not associated only with the marginal ice zone. Indeed, the observations of significant amounts of snow-ice and superimposed ice in ice cores collected during N-ICE2015 [*Granskog et al*., 2017], supports that assumption. We need more measurements and model studies to establish the importance of snow-ice formation in the future Arctic. Indeed the marginal ice zone is expected to encompass the entire Arctic in a seasonally-ice-free Arctic.

Acknowledgments

We deeply thank the crew and scientists on board R/V Lance. Special thanks to Bengt Rotmo and Michel Calzas for assistance with deployment of the buoys. The Finnish Meteorological Institute contributed with three ice mass balance instruments. This work has been supported by the Norwegian Polar Institute's Centre for Ice, Climate and Ecosystems (ICE) through the N-ICE project. N-ICE acknowledges the in-kind contributions provided by other national and international projects and participating institutions, through personnel, equipment, and other support. In particular we acknowledge support from the ANR EQUIPEX IAOOS project, through ANR-10-EQPX-32-01 grant, and the ICE-ARC programme from the European Union 7th Framework Programme, grant 603887. The SIMBA data are available in *Itkin et al.* [2015] and C. Provost (cp@locean-ipsl.upmc.fr).

References

Bintanja, R., and F. M. Selten (2014), Future increases in Arctic precipitation linked to local evaporation and sea-ice-retreat, *Nature*, *509*, 479–484, doi:10.1038/nature13259.

Bitz, C. M., and W. H. Lipscomb (1999), An energy conserving thermodynamic model of sea ice, *J. Geophys. Res.*, *104*, 15,669–15,677.

Boisvert, L. N., and J. C. Stroeve (2015), The Arctic is becoming warmer and wetter as revealed by the Atmospheric Infrared Sounder, *Geophys. Res. Lett.*, *42*, 4439–4446, doi:10.1002/2015GL063775.

Bromwich, D. H., Z. Guo, L. Bai, and Q.-S. Chen (2004), Modeled Antarctic precipitation. Part I: Spatial and temporal variability, *J. Clim.*, *17*, 427–447.

Cohen, L., S. R. Hudson, V. P. Walden, R. M. Graham, and M. A. Granskog (2017), Meteorological conditions in a thinner Arctic sea ice regime from winter to during the Norwegian young sea ICE expedition (N-ICE2015), *J. Geophys. Res. Atmos.*, *122*, doi:10.1002/2016JD026034, in press.

Dee, D. P., et al. (2011), The ERA-Interim reanalysis: Configuration and performance of the data assimilation system, *Q. J. R. Meteorol. Soc.*, *137*(656), 553–597, doi:10.1002/qj.828.

Eicken, H., M. A. Lange, H. W. Hubberten, and P. Wadhams (1994), Characteristics and distribution patterns of snow and meteoric ice in the Weddell Sea and their contribution to the mass balance of sea ice, *Ann. Geophys.*, *12*, 80–93.

Eicken, H., H. Fischer, and P. Lemke (1995), Effects of snow cover on Antarctic sea ice and potential modulation of its response to climate change, *Ann. Glaciol.*, *21*, 369–376.

Golden, K. M., S. F. Ackley, and V. I. Lytle (1998), The percolation phase transition in sea ice, *Science*, *282*, 2238–2241, doi:10.1126/science.282.5397.2238.

Graham, R. M., A. Rinke, L. Cohen, S. R. Hudson, V. P. Walden, M. A. Granskog, W. Dorn, M. Kayser, and M. Maturilli (2017), A comparison of the two Arctic atmospheric winter states observed during N-ICE2015 and SHEBA, *J. Geophys. Res. Atmos.*, *122*, 5716–5737, doi:10.1002/2016JD025475.

Granskog, M., P. Assmy, S. Gerland, G. Spreen, H. Steen, and L. H. Smedsrud (2016), Arctic research on thin ice—Consequences of Arctic sea ice loss, *Eos Trans. AGU*, *97*(5), 22–26, doi:10.1029/2016EO044097.

Granskog, M. A., T. A. Martma, and R. A. Vaikmäe (2003), Development, structure and composition of land-fast sea ice in the northern Baltic Sea, *J. Glaciol.*, *49*(164), 139–148.

Granskog, M. A., A. Rösel, P. A. Dodd, D. V. Divine, S. Gerland, T. Martma, and M. J. Leng (2017), Snow contribution to first-year and second-year Arctic sea ice mass balance north of Svalbard, *J. Geophys. Res. Oceans*, *122*, 2539–2549, doi:10.1002/2016JC012398.

Haapala, J., M. Lensu, M. Dumont, A. H. H. Renner, M. A. Granskog, and S. Gerland (2013), Small-scale horizontal variability of snow, sea-ice thickness and freeboard in the first-year ice region north of Svalbard, *Ann. Glaciol.*, *54*(62), 261–266, doi:10.3189/2013AoG62A157.

Hezel, P. J., X. Zhang, C. M. Bitz, B. P. Kelly, and F. Massonnet (2012), Projected decline in spring snow depth on Arctic sea ice caused by progressively later autumn open ocean freeze-up this century, *Geophys. Res. Lett.*, *39*, L17505, doi:10.1029/2012GL052794.

Hudson, S., L. Cohen, and V. Walden (2016), *N-ICE2015 Surface Meteorology*, Norw. Polar Inst., Tromsø, Norway, doi:10.21334/npolar.2015.056a61d1.

Itkin, P., G. Spreen, S. R. Hudson, M. A. Granskog, S. Gerland, B. Cheng, and H. Steen (2015), *N-ICE2015 Buoy Data [Data Set]*, Norw. Polar Inst., doi:10.21334/npolar.2015.6ed9a8ca.
Itkin, P., G. Spreen, B. Cheng, M. Doble, F. Girard-Ardhuin, J. Haapala, N. Hughes, L. Kaleschke, M. Nicolaus, and J. Wilkinson (2017), Thin ice and storms: Sea ice deformation from buoy arrays deployed during N-ICE2015, *J. Geophys. Res. Oceans*, *122*, 4661–4674, doi:10.1002/2016JC012403, in press.
Jackson, K., J. Wilkinson, T. Maksym, D. Meldrum, J. Beckers, C. Haas, and D. McKenzie (2013), A novel and low-cost sea-ice mass balance buoy, *J. Atmos. Oceanic. Technol.*, *30*, 2676–2688, doi:10.1175/JTECH-D-13-00058.
Jeffries, M. O., A. Worby, K. Morris, and W. F. Weeks (1997), Seasonal variations in the properties and structural composition of sea ice and snow cover in the Bellingshausen and Amundsen Seas, Antarctica, *J. Glaciol.*, *43*, 138–151.
Jeffries, M. O., R. H. Krouse, B. Hurst-Cushing, and T. Maksym (2001), Snow-ice accretion and snow-cover depletion on Antarctic first-year sea-ice floes, *Ann. Glaciol.*, *33*, 51–60.
Kawamura, T., K. Shirasawa, and K. Kobinata (2001), Physical properties and isotopic characteristics of landfast sea ice around the North Water (NOW) Polynya region, *Atmos. Ocean*, *39*(3), 173–182, doi:10.1080/07055900.2001.9649674.
Kirillov, S., I. Dmitrenko, D. Babb, S. Rysgaard, and D. Barber (2015), The effect of ocean heat flux on seasonal ice growth in Young Sound (Northeast Greenland), *J. Geophys. Res. Ocean*, *120*, 4803–4824, doi:10.1002/2015JC010720.
Koenig, Z., C. Provost, N. Villacieros-Robineau, N. Sennéchael, and A. Meyer (2016), Winter ocean-ice interactions under thin sea ice observed by IAOOS platforms during N-ICE 2015: Salty surface mixed layer and active basal melt, *J. Geophys. Res. Oceans*, *121*, 7898–7916, doi:10.1002/2016JC012195.
Lewis, M. J., J. L. Tison, B. Weissling, B. Delille, S. F. Ackley, F. Brabant, and H. Xie (2011), Sea ice and snow cover characteristics during the winter-spring transition in the Bellingshausen Sea: An overview of SIMBA 2007, *Deep Sea Res., Part II*, *58*(9), 1019–1038, doi:10.1016/j.dsr2.2010.10.027.
Lindsay, R., and A. Schweiger (2015), Arctic sea ice thickness loss determined using subsurface, aircraft, and satellite observations, *Cryosphere*, *9*, 269–283, doi:10.5194/tc-9-269-2015.
Maksym, T., and T. Markus (2008), Antarctic sea-ice thickness and snow to ice conversion from atmospheric reanalysis and passive microwave snow depth, *J. Geophys. Res.*, *113*, C02S12, doi:10.1029/2006JC004085.
Maslanik, J. A., C. Fowler, J. Stroeve, S. Drobot, J. Zwally, D. Yi, and W. Emery (2007), A younger, thinner Arctic ice cover. Increased potential for rapid extensive sea-ice loss, *Geophys. Res. Lett.*, *34*, L24501, doi:10.1029/2007GL032043.
Massom, R. A., et al. (2001), Snow on Antarctic sea ice, *Rev. Geophys.*, *39*, 413–445.
Maykut, G. A., and N. Untersteiner (1971), Some results from a time-dependent thermodynamical model of sea-ice, *J. Geophys. Res.*, *76*, 1550–1575.
McPhee, M. G., T. Kikuchi, J. H. Morison, and T. P. Stanton (2003), Ocean-to-ice heat flux at the North Pole environmental observatory, *Geophys. Res. Lett.*, *30*(24), 2274, doi:10.1029/2003GL018580.
Ono, N. (1967), Physics of snow and ice, in *Specific Heat and Heat of Fusion of Sea Ice*, pp. 599–610, Inst. of Low Temp. Sci., Hokkaido, Japan.
Overland, J. E., and M. Wang (2013), When will the summer Arctic be nearly sea ice free?, *Geophys. Res. Lett.*, *40*, 2097–2101, doi:10.1002/grl.50316.
Overland, J. E., M. Wang, J. E. Walsh, J. H. Christensen, V. M. Kattsov, and W. L. Chapman (2012), Climate model projections for the Arctic, in *Snow, Water, Ice and Permafrost in the Arctic*, chap. 3, pp. 3.1–3.18, Arctic Monitoring and Assessment Programme, Oslo.
Perovich, D. K., and J. A. Richter-Menge (2009), Loss of sea ice in the Arctic, *Ann. Rev. Mar. Sci.*, *1*, 417–441, doi:10.1146/annurev.marine.010908.163805.
Pringle, D. J., H. J. Trodahl, and T. G. Haskell (2006), Direct measurements of sea ice thermal conductivity: No surface reduction, *J. Geophys. Res.*, *111*, C05020, doi:10.1029/2005JC0002990.
Rösel, A., et al. (2016), *N-ICE2015 Snow Depth Data With Magna Probe [Data Set]*, Norw. Polar Inst., doi:10.21334/npolar.2016.3d72756d.
Sirevaag, A. (2009), Turbulent exchange coefficients for the ice/ocean interface in case of rapid melting, *Geophys. Res. Lett.*, *36*, L04606, doi:10.1029/2008GL036587.
Spreen, G., R. Kwok, and D. Menemenlis (2011), Trends in Arctic sea ice drift and role of wind forcing: 1992–2009, *Geophys. Res. Lett.*, *38*, L19501, doi:10.1020/2011GL048970.
Tucker, W. B., T. C. Grenfell, R. G. Onstott, D. K. Perovich, A. J. Gow, R. A. Shuchman, and L. L. Sutherland (1991), Microwave and physical properties of sea ice in the winter marginal ice zone, *J. Geophys. Res.*, *96*, 4573–4587, doi:10.1029/90JC02269.
Ukita, J., T. Kawamura, N. Tanaka, T. Toyota, and M. Wakatsuchi (2000), Physical and stable isotopic properties and growth processes of sea ice collected in the southern Sea of Okhotsk, *J. Geophys. Res.*, *105*, 22,083–22,093.
Vihma, T., et al. (2014), Advances in understanding and parameterization of small-scale physical processes in the marine Arctic climate system: A review, *Atmos. Chem. Phys.*, *14*, 9403–9450, doi:10.5194/acp-14-9403-2014.
Webster, M. A., I. G. Rigor, S. V. Nghiem, N. T. Kurtz, S. L. Farrell, D. K. Perovich, and M. Sturm (2014), Interdecadal changes in snow depth on Arctic sea ice, *J. Geophys. Res. Oceans*, *119*, 5395–5406, doi:10.1002/2014JC009985.
Warren, S. G. et al. (1999), Snow depth on Arctic sea ice, *J. Clim.*, *12*, 1814–1829.
Weeks, W. F., and O. S. Lee (1958), Observations on the physical properties of sea-ice at Hopedale, Labrador, *Arctic*, *11*(3), 135–155.
Worby, A. P., C. A. Geiger, M. J. Pager, M. L. Van Woert, S. F. Ackley, and T. L. DeLiberty (2008), The thickness distribution of Antarctic sea ice, *J. Geophys. Res.*, *113*, C05592, doi:10.1029/2007JC004254.
Yen, Y. C. (1981), Review of thermal properties of snow, ice and sea ice, *Rep. 81-10*, 27 pp., U.S. Army Cold Reg. Res. and Eng. Lab., Hanover, N. H.